LETTER

Microtearing turbulence limiting the JET-ILW pedestal

To cite this article: D.R. Hatch *et al* 2016 *Nucl. Fusion* **56** 104003

View the article online for updates and enhancements.

Letter

Microtearing turbulence limiting the JET-ILW pedestal

D.R. Hatch[1], M. Kotschenreuther[1], S. Mahajan[1], P. Valanju[1], F. Jenko[2], D. Told[2], T. Görler[3] and S. Saarelma[4]

[1] Institute for Fusion Studies, University of Texas at Austin, Austin, TX 78712, USA
[2] Department of Physics and Astronomy, University of California, Los Angeles, CA 90095, USA
[3] Max Planck Institute for Plasma Physics, Boltzmannstr. 2, 85748 Garching, Germany
[4] Culham Centre for Fusion Energy, Culham Science Centre, Abingdon OX14 3DB, UK

E-mail: drhatch@austin.utexas.edu

Abstract
The first nonlinear gyrokinetic turbulence simulations that quantitatively reproduce experimental transport levels in an H-mode pedestal are reported. In the JET-ILW (ITER-like wall) pedestal, the bulk of the transport in the steep gradient region is caused by the turbulence driven by the microtearing mode (MTM). Kinetic ballooning modes are found to be in a second-stability regime. With contributions from the neoclassical and electron temperature gradient driven transport, the MTM mechanism reproduces, quantitatively, the experimental power balance across most of the pedestal.

Keywords: pedestal, gyrokinetics, microtearing mode, JET, ITER-like wall

(Some figures may appear in colour only in the online journal)

Introduction

The tokamak H-mode [1] is defined by a narrow insulating region—the pedestal—at the plasma edge, where turbulence is suppressed and sharp pressure gradients develop. The pedestal is at the center of the most pressing issues facing fusion energy. ITER, for example, must reach a sufficient temperature at the pedestal's inner boundary in order to achieve its fusion power targets [2]. This work reports the results of, perhaps, the very first, first-principles simulations of the H-mode pedestal dynamics that reproduce experimentally observed transport levels.

This study targets the JET-ILW (ITER-like wall) pedestal [3–5], which approaches ITER conditions in two important ways: (1) as the largest tokamak in operation, it most-closely approximates plasma parameters that are dependent on machine size (like ρ_*, the ratio of the gyro-radius to minor radius), (2) to approximate ITER conditions even better, JET has recently installed an ITER-like wall (ILW) (composed of a tungsten divertor and beryllium chamber). This modification substantially decreases the global confinement, attributable largely to striking changes in pedestal structure. Hence, it is critically important, for both JET operation and ITER's prospects, to develop an understanding of the mechanisms underlying JET-ILW pedestal dynamics.

In this work, we elucidate the mechanisms limiting profile evolution in a representative JET-ILW discharge. We demonstrate, through simulations using the gyrokinetic code GENE [6, 7], that the microtearing mode [8–15] (MTM) is the dominant instability in the pedestal. Most importantly, we determine via nonlinear gyrokinetic simulations that the MTM-driven turbulence, in combination with electron temperature gradient (ETG) [6, 16–19] driven turbulence and neoclassical flux, produces transport levels closely matching experimental power balance across most of the pedestal, demonstrating the capacity of these mechanisms to limit JET-ILW pedestal evolution.
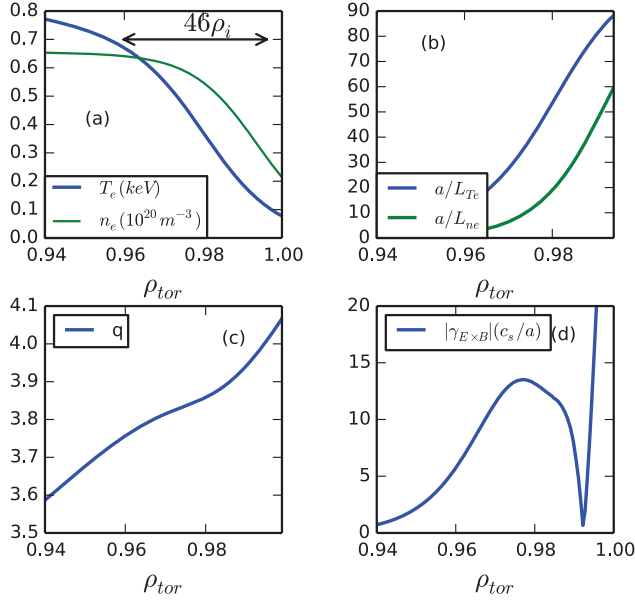
Figure 1. Electron density and temperature profiles (identical to ion profiles except where stated otherwise in the text) (*a*), the normalized inverse gradient scale lengths $a/L_{T,n} = \frac{d}{d\rho_{tor}} \ln(T, n)$ (*b*), the safety factor q (*c*), and the Hahm–Burrell shear rate [46] (*d*). The arrow in (*a*) denotes a region of the pedestal corresponding to 46 ion gyroradii (with gyro-radius calculated at $\rho_{tor} = 0.98$).

The JET-ILW pedestal

JET pulse 82585 (high triangularity $\delta = 0.38$, $I = 2.5$ MA, $B = 2.7$ T—described in [3]) is part of an experimental campaign studying the effect of deuterium fueling on pedestal structure. In this series of discharges, the pedestal broadens but does not heighten with increasing fueling rate. This behavior is contrary to the expected [20, 21] scaling of pedestal width with plasma pressure—typically $\Delta \propto \sqrt{\beta_{pol}}$, where Δ is the pedestal width, $\beta_{pol} = 2\mu_0 P/B_{pol}^2$, P is pressure, and B_{pol} is the poloidal magnetic field. In order to model the transport in this JET-ILW pedestal, we have reproduced the pre-ELM temperature and density profiles, along with the shape of the outer flux surface from data reported in [3]. The necessary gyrokinetic inputs (radial profiles of density and temperature, magnetic equilibrium, and background flow profile) are self-consistently constructed using the equilibrium code VMEC in conjunction with neoclassical formulas [22] for the bootstrap current and radial electric field. In GENE, the effect of $E \times B$ shear enters through the advective derivative associated with the toroidal rotation (with different treatments in the flux tube and global implementations [23]). Here we take the toroidal rotation to be $\Omega_{tor} = \frac{E_r}{RB_\theta}$, consistent with an $E \times B$ flow whose advective derivative is negligible in the direction parallel to the magnetic field. Figure 1 shows the density and temperature profiles (a), the normalized inverse gradient scale lengths $a/L_{T,n} = \frac{d}{d\rho_{tor}} \ln(T, n)$ (b), the safety factor q (c), and the Hahm–Burrell shear rate [46] (d). For reference, the pedestal top value of β is $\beta_e = 8\pi n_{e0}T_{e0}/B^2 = 2.4 \times 10^{-3}$. Due to considerable uncertainty in the ion temperature, we assume

it to be equal to the electron temperature (sensitivity tests are described below). We also take the ion and electron density profiles to be equal, consistent with the low values of Z_{eff} characteristic of unseeded JET-ILW discharges. Further variations are the topic of ongoing research and are reported elsewhere [47, 48].

Pedestal instabilities

A host of instabilities has been proposed or identified in H-mode pedestals in both experiment and theory [24]. Experimentally, fluctuations have been diagnosed that are consistent with MTM [25, 26, 28], KBM [25, 27–29], and trapped electron modes (TEM) [25], while linear gyrokinetic modeling has identified MTM [30–34], TEM [34, 35], ETG [33, 34, 36, 37], KBM [29, 30, 32–34, 38, 39], and generically-classified drift waves [40]. The EPED model appeals exclusively to KBM as the effective local pedestal-limiting instability [20]. Notably, in the context of the present research, MTM has been proposed as a pedestal fluctuations based on linear analytic theory [41–43]. Due to the large number of instabilities identified, and the complexity of the nonlinear turbulent state (which reflects the underlying instabilities in not-so-obvious ways), no clear picture has emerged regarding the relative role of these modes with respect to pedestal transport and structure. The identification of such a wide array of linear instabilities in gyrokinetic studies underscores the necessity of nonlinear simulations to clarify the relevant transport mechanisms. Such an analysis will be presented below following the present accounting of the linear instabilities in the JET-ILW pedestal.

The modes identified in our linear simulations of the JET-ILW pedestal may be classified into three distinct categories—MTM, KBM, and electrostatic drift waves (ESDW) (encompassing, e.g. ITG and TEM) with the following defining characteristics: (1) the KBM is identified by a positive (ion direction) frequency, ballooning parity (predominantly symmetric [antisymmetric] mode structure for ϕ [$A_\parallel$] along the field line), and a near-vanishing $E_\parallel = -\partial_z\phi + i\omega A_\parallel$ (expected for a mode largely determined by ideal MHD) as quantified by the ratio

$$\hat{E}_\parallel = \frac{\int dz |-\partial_z\phi + i\omega A_\parallel|}{\int dz |\partial_z\phi| + \int dz |i\omega A_\parallel|}, \qquad (1)$$

where ϕ is the electrostatic potential, z is the coordinate parallel to the background magnetic field, ω is the complex mode frequency, and $A_\parallel$ is the parallel magnetic vector potential. KBM were determined to have values of $\hat{E}_\parallel$ typically below 0.1; (2) the MTM is identified by mode structures with predominantly tearing parity (opposite of ballooning parity), negative (electron direction) frequencies, and dominantly electromagnetic transport as quantified by the ratio (Q_e^{EM}/Q^{ES}) of the electron electromagnetic heat flux to the electrostatic heat fluxes, all calculated from the linear eigenmodes; (3) all modes not encompassed by the MTM/KBM criteria are categorized as ESDW. The MTM and KBM instabilities are
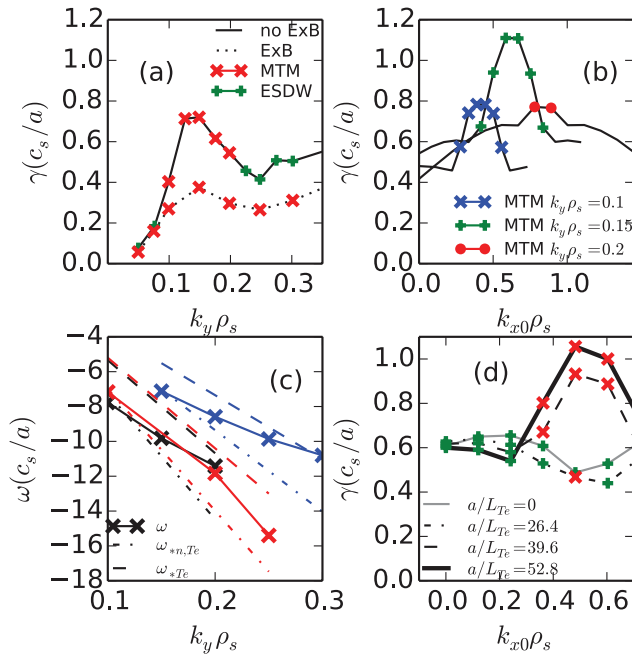
Figure 2. Global growth rates with and without $E \times B$ shear (*a*), dependence of local MTM growth rates on central k_x (i.e. ballooning angle) (*b*), mode frequency of MTM modes for various cases (global and local at different radial locations) in comparison with ω_* (*c*), and a scan in electron temperature gradient scale length a/L_{Te} and central k_x for $k_y\rho_s = 0.15$.

Figure 3. Structure of $A_\parallel$ for a linear global MTM eigenmode without shear flow. The eigenmode peaks at the top and bottom (shown) of the tokamak, is limited to a narrow radial band, and is characterized by fine-scale radial structure. These features serve to reduce the effect of shear on the MTM.

manifest at low k_y, whereas ESDW are always unstable across a broad range of scales ranging from ion-scales to electron scales (ETG).

The GENE code was used in both its local and (more comprehensive) global modes of operation. Simulations include the Landau–Boltzmann collision operator, electromagnetic effects, and fully-realistic geometry. Parallel magnetic fluctuations are included in local but not global simulations. In global simulations, the effects of parallel magnetic fluctuations are approximated by setting the ∇B drift equal to the curvature drift [44, 45]—a treatment that has previously been demonstrated to accurately capture KBM stability and was verified to do so in this case by calculations with the local code. In the following, z denotes the coordinate along the field line, y denotes the binormal direction, and x is the radial direction. The typical numerical resolution used for these linear simulations was (48–96, 48, 16) grid points in the ($z, v_\parallel, \mu$) coordinates, where $v_\parallel$ is the parallel velocity and μ is the magnetic moment (proportional to perpendicular velocity squared). Typically 256 radial grid points (for a ~ 46 ion gyro radii box) were used for global simulations and 13 k_x wave numbers for local simulations.

Local simulations identify MTM as the dominant low-k_y instability over most of the pedestal (from the pedestal top to $\rho_{tor} = 0.988$), with KBM unstable in the region $\rho_{tor} > 0.988$. Notably, the MTM is only the most unstable mode at finite k_x (closely related to the ballooning angle θ_0 in ballooning theory) as seen in figure 2(*b*). As a result, this MTM instability would be missed by analyses (often standard) sampling only $k_x = 0$. Several tests were performed in order to conclusively identify the mode as MTM. As expected for MTM, the
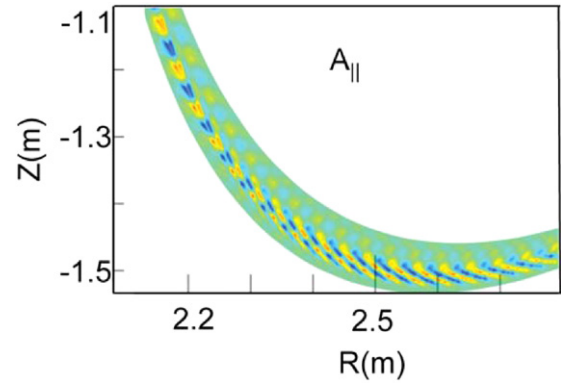
mode frequency is in the electron direction and very close to $\omega_{*n,Te} = k_y\rho_s c_s(1/L_n + 1/L_{Te})$, as seen in figure 2(*c*). Parameter scans determine that MTM growth rates increase strongly with electron temperature gradients (see figure 2(*d*)), and are weakly suppressed by density and ion temperature gradients. The MTM exhibits moderate cancellation in $E_\parallel$ ($\hat{E}_\parallel \gtrsim 0.3$ being typical), although the electrostatic component of the mode is not crucial to its existence; the MTM growth rate smoothly decreases to $\sim 55\%$ of its nominal value when the amplitude of the electrostatic potential is artificially reduced toward $\phi = 0$. Other mode properties (e.g. $A_\parallel$ mode structure, and frequency) remain unchanged. However, when $A_\parallel$ is analogously reduced, the MTM transforms into a qualitatively distinct ESDW with a growth rate reduced to $\sim 30\%$ of the MTM growth rate.

A more-comprehensive global analysis also identifies the MTM as the dominant instability. In global simulations encompassing the entire pedestal (with boundaries at $\rho_{tor} = 0.9605$ and $\rho_{tor} = 0.9995$) the KBM is not manifest, while the MTM persists with growth rates roughly comparable to the radially-averaged local MTM growth rates. MTM growth rates decrease in the presence of $E \times B$ shear flow, but to a lesser degree than the surrounding ESDW as shown in figure 2(*a*). The mode structure of the MTM eigenmode (shown in figure 3) elucidates the source of its relative insensitivity to shear flow. The MTM magnetic vector potential $A_\parallel$ mode structure peaks at the top and bottom of the tokamak where flux surfaces are broadly spaced, is radially localized, and has fine radial structure. All these features contribute to a lower effective shear rate [46]. Ongoing work is studying the susceptibility of various modes to shear flow and will be reported elsewhere [47].

Pedestal β scan

In light of experimental uncertainties and the dynamic nature of pedestal evolution, we repeat the above analysis over a series of fully self-consistent equilibria scanning values of β about the nominal experimental value (the analogous density scan produced qualitatively similar results). In addition
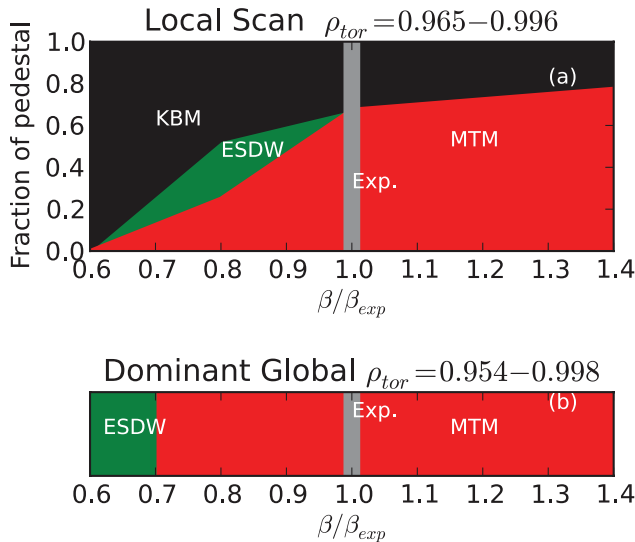
Figure 4. Fraction of the pedestal unstable to KBM, MTM, and ESDW in local gyrokinetic simulations (*a*), and the dominant low-k_y ($k_y\rho_s < 0.5$) instability in global simulations (*b*) over a range of β surrounding the experimental operating point. MTM becomes increasingly dominant as β increases, while KBM is in a second-stability regime, becoming less prominent as β increases. MTM persists in global simulations, while KBM is subdominant. The scan uses fully self-consistent equilibria for each β point.

to gauging the sensitivity of our results, such a scan can be roughly conceptualized as sampling the inter-ELM evolution of the pedestal, during which the pressure profile recovers from an ELM collapse and returns to its pre-ELM level.

The β scan was constructed by varying the pedestal top temperature from 60% to 140% of its nominal experimental value and producing fully self-consistent equilibria for each scan point. Local linear results, summarized in figure 4(*a*), show the fraction of the pedestal over which KBM and MTM are unstable. KBM is identified across the entire pedestal in the low-β regime but becomes more stable and limited to progressively narrower regions as β increases toward and beyond the experimental value. In contrast, MTM becomes unstable at β values slightly below the experimental operating point and becomes more pronounced as β increases. This trend suggests that the MTM becomes more robustly unstable over the course of an ELM cycle, as would be expected for the dominant mode limiting profile evolution. In contrast, the KBM becomes increasingly stable and limited to a narrow region at the far edge. This picture of local KBM stability is consistent with other studies demonstrating that KBM is in the so-called second stability regime in JET [32] and NSTX [33] pedestals.

Global simulations reinforce the picture drawn by the local analysis. In figure 4(*b*), displaying the dominant global mode over the β scan, MTM is seen to be dominant in a broad region of parameter space; at low β, it is replaced not by KBM but rather ESDW. In other words, a fully global treatment identifies KBM to be subdominant even in cases where a local analysis finds robust KBM instability across the entire pedestal. KBM instability can only be recovered in global simulations by increasing the simulation box (far beyond the width of the pedestal) while artifically maintaining steep gradients

across the box. This suggests that the local analysis that is often relied upon to identify KBM stability boundaries may be inadequate. Large differences between global and local eigenvalue treatments for a given mode (as described above) are not unique to this scenario. Such a behavior is illustrated, for example, in [49], which deals with the global versus local stability for magneto-rotational instability.

It should be noted that the gyrokinetic model does not include the kink term (relevant for kink-peeling instability). Although it cannot be ruled out as a potential destabilizing effect, the term has been implemented in gyrokinetic codes [39, 50] and was not found to be important in the pedestal [39].

Nonlinear turbulent transport

Having characterized the linear instabilities at and near the experimental operating point, one must calculate their consequences for the nonlinear turbulent state. Of particular importance is the question whether the nonlinear turbulent transport produced by the MTM can account for experimental power balance and by extension the structure of the pedestal. To this end, extensive nonlinear simulations were performed. GENE was used primarily in a local mode of operation, employing a real space radial coordinate with Dirichlet boundary conditions, while keeping plasma parameters and gradients constant across the box. This approach was benchmarked against global simulations where possible; a nonlinear global simulation with $k_{y,\min}\rho_s = 0.05$ produced transport levels differing by $\sim$10% from the corresponding local simulation, consistent with earlier work suggesting MTM is rather insensitive to global effects [51]. Nonlinear global simulations could not be extended to lower k_y due to numerical issues (likely resolvable with higher resolution simulations that are beyond the scope of this work). Simulations used (256, 48, 48, 16) gridpoints in the $(x, z, v_\parallel, \mu)$ coordinates—values established by extensive convergence tests. Transport quantities were most sensitive to resolution in the y coordinate, converging at $k_{y,\min}\rho_s = 0.018$, while resolving up to to $k_{y,\max}\rho_s = 1.71$. The radial resolution is sufficient for approximately six grid points per rational surface for the maximum toroidal mode number in the simulation ($n = 475$) (note that the magnetic shear $\hat{s}$ is approximately 1.1 for the case described below).

As expected for MTM-driven turbulence, nonlinear simulations show heat flux predominantly in the electron electromagnetic channel ($\sim$63%). The remainder (37%) of the heat flux is electrostatic, and becomes dominant at higher temperature and/or lower ρ_*, as described in [47, 48]. All comparisons indicate that the turbulence is the nonlinear manifestation of the underlying MTM instability. The insensitivity of the MTM to shear suppression is also observed in the nonlinear simulations; as a test, the turbulence was evolved shear-free to a saturated state at which point the shear was turned on. The shear flow reduced the electrostatic component (ESDW) of the flux by orders of magnitude while the electromagnetic component (MTM) was reduced by a factor of $\sim$2, roughly consistent with the decrease in growth rates shown in figure 2(*a*).

Several tests were conducted in order to probe the sensitivity of the transport levels to various numerical parameters and physical uncertainties. Tests demonstrated insensitivity of transport quantities to radial box size (increased from 0.022 of the minor radius to 0.029), increased resolution in $(z, v_\parallel, \mu)$, increased $k_{y,max}$, and use of k_y hyperdiffusivity (damping proportional to $(k_y/k_{y,max})^4$). The uncertainty in the estimated $E \times B$ shear was probed by (1) decreasing the shear rate by 25% and (2) allowing the shear rate to vary over the box (while preserving the local approximation for all other quantities). These modifications produced moderate increases in transport (20–30% in the electrostatic channel), while negligibly affecting the dominant electromagnetic channel. MTM growth rates were found to be insensitive to ion temperature variations (probed by considering a case with increased ion separatrix temperature—from 80 eV to 300 eV). Although we did not quantify the effect, ETG transport is expected to increase somewhat with increased temperature ratio T_i/T_e.

Single scale (adiabatic ions) ETG simulations were also carried out. Numerical parameters were established by convergence tests: 384, 48, 16 grid points in the $z, v_\parallel, \mu$ coordinates, with 128 Fourier modes for the x coordinate (resolving from $k_{x,min}\rho_s = 2.15$ to $k_{x,max}\rho_s = 138$) and 48 (non-negative) Fourier modes in the y coordinate resolving from (resolving from $k_{x,min}\rho_s = 5$ to $k_{x,max}\rho_s = 235$). The most unique numerical aspect of these simulations is the requirement to use very high parallel resolution to resolve fine-scale parallel structures. In the discussion below, we make the assumption that ion-scale and electron-scale fluxes are a reasonable proxy for authentic multiscale simulations [52–58], which are beyond the scope of this work. Although modified heat fluxes due to inter-scale coupling cannot be ruled out, the major multiscale coupling mechanisms identified in the literature are expected to be less-relevant due to the unique features of the pedestal turbulence described here: (1) the ETG fluctuations are isotropic (as also observed in [23, 34]) rather than streamer-dominated and so would be expected to be less-susceptible to shearing from ion-scale fluctuations [56, 58], and (2) the ion-scale turbulence is mediated by external shear flow as opposed to zonal flows, which can be sensitive to ETG-scale fluctuations [56]. Moreover, the maximum ETG growth rates exceed the maximum ion-scale growth rates by a factor somewhat exceeding the square root of the mass ratio, which has been identified as a criterion indicating when ETG fluctuations become largely independent from ion-scale interaction [54, 58].

Three radial locations were selected for detailed analysis: $\rho_{tor} = 0.97$ near the pedestal top, $\rho_{tor} = 0.98$ in the steep gradient region, and $\rho_{tor} = 0.99$ at the far edge. The far outer point produced transport levels ~3 times lower than nominal power balance. Higher transport could certainly be achieved by adjusting the background profiles within experimental error bars, but such a course was not pursued due to the severe uncertainties intrinsic to this far edge region (e.g. potential power losses due to charge exchange, uncertainty in separatrix position, and effects associated with close proximity to the open field line region). Simulation results at the other radial locations reproduce experimental power balance strikingly well as shown in figure 5. MTM-dominated turbulence at
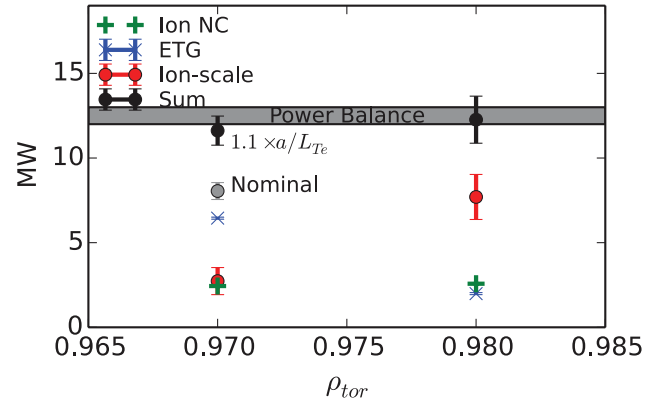

Figure 5. Contributions to the heat transport from ion neoclassical (green pluses), ETG (blue Xs), and MTM (red circles) at two radial locations, demonstrating agreement with experimental power balance. MTM is dominant in the steep gradient region while ETG is dominant near the pedestal top where η_e is large.

$\rho_{tor} = 0.98$ produces ~7.5 MW of transport, single-scale simulations of ETG turbulence produce an additional ~2 MW, and calculations of neoclassical transport predict 2.5 MW (ions). The combination amounts to ~12 MW, compared to 12–13 MW estimated experimentally (16 MW neutral beam heating and 3–4 MW radiation losses in the core). Simulations at $\rho_{tor} = 0.97$ are dominated by ETG transport (due to the large value of η_e—see figure 1(b)) with MTM and neoclassical playing a smaller role. Power balance is again satisfied, requiring only a minor adjustment (10% increase) to the electron temperature gradient.

We briefly make some general observations regarding profile stiffness. As described above, the simulations with an increased electron temperature gradient (at $\rho_{tor} = 0.97$) exhibit a 44% increase in total transport (from 8.1 to 11.6 MW) caused by a 10% increase in a/L_{Te}. More specifically, the ETG transport increases from 4.6 to 6.5 MW and the ion scale (MTM-dominated) heat flux nearly doubles (from 1.4 to 2.7 MW). We note also that gyrokinetic simulations based on an AUG pedestal scenario exhibit very strong stiffness—increases in transport of an order of magnitude caused by moderate gradient adjustments (to both electron temperature and density) [34]. Altogether, these observations support the notion that these instabilities provide a mechanism sufficient to limit electron temperature gradients. However, the interplay between the two mechanisms may not translate in a simple manner into a critical gradient criterion due to their distinct parameter dependences, notably a strong dependence on density gradient (via η_e) for ETG.

Broader connections

Finally, we note some compelling connections with magnetic fluctuation data from recent ASDEX-Upgrade (AUG) experiments [59]; the pedestal electron temperature gradient saturates during the inter-ELM cycle simultaneous with the onset of high frequency (near ω_*) fluctuations having comparable intensity on the inboard/outboard sides of the tokamak. For our simulations, the inboard fluctuation amplitude

is approximately twice the outboard level (in contrast with a KBM or a conventional core MTM, which would strongly peak on the outboard). Moreover, the MTM is driven by the electron temperature gradient (recall figure 2(*d*)) and produces predominantly electron heat transport—precisely the properties expected for a mode that arrests the electron temperature pedestal evolution as observed in AUG. Notably, the AUG density pedestal saturates earlier in the ELM cycle, apparently via a separate (low-n) mechanism. The observed frequencies are also potentially consistent with an MTM, depending on the localization of the mode in the pedestal. In summary, our MTM simulations have many features in common with the AUG data, suggesting that MTM pedestal activity may be important in a broader range of pedestal scenarios. Gyrokinetic studies of this and related AUG discharges will be a topic of future work.

Summary and discussion

We demonstrate that the combination of MTM and ETG turbulence along with neoclassical transport is sufficient to account for power balance across most of the JET-ILW pedestal. Electrostatic ion-scale instabilities are strongly shear suppressed, while KBM is insignificant in a broad region of parameter space surrounding the experimental operating point. The close agreement between transport predictions via nonlinear gyrokinetic simulations and experimental pedestal transport levels suggests that gyrokinetic simulations have the capacity to model important aspects of pedestal transport. Additionally, this work lays a foundation for continued study of the JET-ILW pedestal (to be reported in [48]), notably, the trends related to fueling levels and impurity content that impede JET-ILW discharges from achieving high pedestal temperatures.

Acknowledgments

References

[1] Wagner F. *et al* 1982 *Phys. Rev. Lett.* **49** 1408
[2] Doyle E.J. *et al* 2007 Progress in the ITER Physics Basis Chapter 2: Plasma confinement and transport *Nucl. Fusion* **47** S18
[3] Leyland M.J. *et al* 2015 *Nucl. Fusion* **55** 013019
[4] Maggi C.F. *et al* 2015 *Nucl. Fusion* **55** 113031
[5] Giroud C. *et al* 2015 *Plasma Phys. Control. Fusion* **57** 035004
[6] Jenko F., Dorland W., Kotschenreuther M. and Rogers B.N. 2000 *Phys. Plasmas* **7** 1904
[7] Görler T., Lapillonne X., Brunner S., Dannert T., Jenko F., Merz F. and Told D. 2011 *J. Comput. Phys.* **230** 7053
[8] Hazeltine R.D. *et al* 1975 *Phys. Fluids* **18** 1778
[9] Applegate D.J. *et al* 2004 *Phys. Plasmas* **11** 5085
[10] Applegate D.J., Roach C.M., Connor J.W., Cowley S.C., Dorland W., Hastie R.J. and Joiner N. 2007 *Phys. Control. Fusion* **49** 1113
[11] Doerk H., Jenko F., Pueschel M.J. and Hatch D.R. 2011 *Phys. Rev. Lett.* **106** 155003
[12] Guttenfelder W., Candy J., Kaye S.M., Nevins W.M., Wang E., Bell R.E., Hammett G.W., LeBlanc B.P., Mikkelsen D.R. and Yuh H. 2011 *Phys. Rev. Lett.* **106** 155004
[13] Hatch D.R., Pueschel M.J., Jenko F., Nevins W.M., Terry P.W. and Doerk H. 2012 *Phys. Rev. Lett.* **108** 235002
[14] Hatch D.R., Pueschel M.J., Jenko F., Nevins W.M., Terry P.W. and Doerk H. 2013 *Phys. Plasmas* **20** 012307
[15] Chowdhury J., Chen Y., Wan W., Parker S.E., Guttenfelder W. and Canik J.M. 2016 *Phys. Plasmas* **23** 012513
[16] Horton W., Hong B.G. and Tang W.M. 1988 *Phys. Fluids* **31** 2971
[17] Dorland W., Jenko F., Kotschenreuther M. and Rogers B.N. 2000 *Phys. Rev. Lett.* **85** 5570
[18] Jenko F. and Dorland W. 2002 *Phys. Rev. Lett.* **89** 225001
[19] Nevins W.M. *et al* 2006 *Phys. Plasmas* **13** 122306
[20] Snyder P.B., Aiba N., Beurskens M., Groebner R.J., Horton L.D., Hubbard A.E., Hughes J.W., Huysmans G.T.A., Kamada Y. and Kirk A. 2009 *Nucl. Fusion* **49** 085035
[21] Snyder P.B., Groebner R.J., Leonard A.W., Osborne T.H. and Wilson H.R. 2009 *Phys. Plasmas* **16** 056118
[22] Sauter O., Angioni C. and Lin-Liu Y.R. 1999 *Phys. Plasmas* **6** 2834–9
[23] Told D. 2012 *PhD Thesis* Universität Ulm
[24] Groebner R.J. *et al* 2013 *Nucl. Fusion* **53** 093024
[25] Smith D.R., Fonck R.J., McKee G.R., Thompson D.S., Bell R.E., Diallo A., Guttenfelder W., Kaye S.M., LeBlanc B.P. and Podesta M. 2013 *Phys. Plasmas* **20** 055903
[26] Manz P., Boom J.E., Wolfrum E., Birkenmeier G., Classen I.G.J., Luhmann N.C. Jr, Stroth U. and the ASDEX Upgrade Team 2014 *Plasma Phys. Control. Fusion* **56** 035010
[27] Yan Z., McKee G.R., Groebner R.J., Snyder P.B., Osborne T.H. and Burrell K.H. 2011 *Phys. Rev. Lett.* **107** 055004
[28] Yan Z., McKee G.R., Groebner R.J., Snyder P.B., Osborne T.H., Beurskens M.N. and Burrell K.H. 2011 *Phys. Plasmas* **18** 056117
[29] Diallo A. *et al* and Alcator C-Mod team 2014 *Phys. Rev. Lett.* **112** 115001
[30] Dickinson D., Roach C.M., Saarelma S., Scannell R., Kirk A. and Wilson H.R. 2012 *Phys. Rev. Lett.* **108** 135002
[31] Dickinson D., Roach C.M., Saarelma S., Scannell R., Kirk A. and Wilson H.R. 2013 *Plasma Phys. Control. Fusion* **55** 074006
[32] Saarelma S., Beurskens M.N.A., Dickinson D., Frassinetti L., Leyland M.J., Roach C.M. and EFDA-JET Contributors 2013 *Nucl. Fusion* **53** 123012
[33] Canik J.M., Guttenfelder W., Maingi R., Osborne T.H., Kubota S., Ren Y., Bell R.E., Kugel H.W., LeBlanc B.P. and Souhkanovskii V.A. 2014 *Nucl. Fusion* **53** 113016
[34] Hatch D.R., Told D., Jenko F., Doerk H., Dunne M.G., Wolfrum E., Viezzer E., ASDEX Upgrade Team and Pueschel M.J. 2015 *Nucl. Fusion* **55** 063028
[35] Fulton D.P., Lin Z., Holod I. and Xiao Y. 2014 *Phys. Plasmas* **21** 042110
[36] Told D., Jenko F., Xanthopoulos P., Horton L.D., Wolfrum E. and ASDEX Upgrade Team 2008 *Phys. Plasmas* **15** 102306

[37] Jenko F., Told D., Xanthopoulos P., Merz F. and Horton L.D. 2009 *Phys. Plasmas* **16** 055901

[38] Wan W., Parker S.E., Chen Y., Yan Z., Groebner R.J. and Snyder P.B. 2012 *Phys. Rev. Lett.* **109** 185004

[39] Wan W., Parker S.E., Chen Y., Groebner R.J., Yan Z., Pankin A.Y. and Kruger S.E. 2013 *Phys. Plasmas* **20** 055902

[40] Wang E., Xu X., Candy J., Groebner R.J., Snyder P.B., Chen Y., Parker S.E., Wan W., Lu G. and Dong J.Q. 2012 *Nucl. Fusion* **52** 103015

[41] Lau Y.-T. 1990 *Nucl. Fusion* **30** 934

[42] Lau Y.-T. 1996 *Nucl. Fusion* **36** 965

[43] Kesner J. and Migliuolo S. 1999 *Nucl. Fusion* **39** 163

[44] Waltz R.E. and Miller R.L. 1999 *Phys. Plasmas* **6** 4265

[45] Joiner N., Hirose A. and Dorland W. 2010 *Phys. Plasmas* **7** 72104

[46] Hahm T.S. and Burrell K.H. 1995 *Phys. Plasmas* **2** 1648

[47] Kotschenreuther M. *et al* 2016 in preparation

[48] Hatch D.R. *et al* in preparation

[49] Mahajan S.M. and Krishan V. 2008 *Astrophys. J.* **682** 602

[50] Deng W., Lin Z. and Holod I. 2012 *Nucl. Fusion* **52** 023005

[51] Doerk H., Jenko F., Görler T., Told D., Pueschel M.J. and Hatch D.R. 2012 *Phys. Plasmas* **19** 055907

[52] Jenko F. 2004 *J. Plasma Fusion Res. Ser.* **6** 11

[53] Candy J., Waltz R.E., Fahey M.R. and Holland C. 2007 *Plasma Phys. Control. Fusion* **49** 1209

[54] Görler T. and Jenko F. 2008 *Phys. Rev. Lett.* **100** 185002

[55] Görler T. and Jenko F. 2008 *Phys. Plasmas* **15** 102508

[56] Maeyama S., Idomura Y., Watanabe T.-H., Nakata M., Yagi M., Miyato N., Ishizawa A. and Nunami M. 2015 *Phys. Rev. Lett.* **114** 255002

[57] Howard N.T., Holland C., White A.E., Greenwald M. and Candy J. 2016 *Nucl. Fusion* **56** 14004

[58] Howard N.T., Holland C., White A.E., Greenwald M., Candy J. and Creely A.J. 2016 *Phys. Plasmas* **23** 56109

[59] Laggner F.M. *et al*, the EUROfusion MST1 Team and the ASDEX Upgrade Team 2016 *Plasma Phys. Control. Fusion* **58** 65005